

Highlights

Impacts of Hurricane Irma (2017) on ocean transport processes

Thomas Dobbelaere, Milan Curcic, Matthieu Le Hénaff, Emmanuel Hanert

- The coupled SLIM+SWAN model correctly reproduces the hydrodynamics and waves during Irma.
- Wave radiation stress increases currents by up to 1 m/s during Irma.
- Wave radiation stress gradients are the largest on the shelf break and over reefs.
- Waves can deflect drifting particles by up to 20 km during the hurricane.
- The Stokes drift has a larger impact on transport than the wave radiation stress.

Impacts of Hurricane Irma (2017) on ocean transport processes

Thomas Dobbelaere^{a,*}, Milan Curcic^b, Matthieu Le Hénaff^{c,d}, Emmanuel Hanert^{a,e}

^a*Eath and Life Institute (ELI), UCLouvain, Louvain-la-Neuve, Belgium*

^b*Rosenstiel School of Marine and Atmospheric Sciences (RSMAS), University of Miami, Coral Gables, Florida, USA*

^c*Cooperative Institute for Marine and Atmospheric Studies (CIMAS), University of Miami, Miami, Florida, USA*

^d*Atlantic Oceanographic and Meteorological Laboratory (AOML), NOAA, Miami, Florida, USA*

^e*Institute of Mechanics, Materials and Civil Engineering (IMMC), UCLouvain, Louvain-la-Neuve, Belgium*

Abstract

The frequency of major tropical cyclones has increased during the past decade. Their effect is particularly acute in coastal areas where they cause extensive damage leading to an influx of debris, sediments and waste to the sea. However, the default setting of most operational coastal ocean models do not represent heavy-wind transport processes correctly as they do not couple the hydrodynamics with the wind-generated waves. This may lead to significant errors in ocean simulations under tropical cyclone conditions. Here, we investigate current-wave interactions during a major hurricane and assess their impact on transport processes. We do that by coupling the unstructured-mesh coastal ocean model SLIM with the spectral wave model SWAN, and applying it to the Florida Reef Tract during Hurricane Irma (September 17). We show that the coupled model successfully reproduces the wave behavior, the storm surge and the ocean currents during the passage of the hurricane. We then

*Corresponding author

Email address: thomas.dobbelaere@uclouvain.be (Thomas Dobbelaere)

use the coupled and uncoupled wave-current model to simulate the transport of passive drifters. We show that the wave radiation stress gradient alone can lead to changes of up to 1 m/s in the modeled currents, which in turn leads to differences of up to 5 km in the position of drifting material over the duration of the hurricane. The Stokes drift however appears to cause deflections up to 4 times more intense and should thus be considered in priority. Wave-current interactions therefore strongly impact the transport of drifting material such as sediments and debris in the aftermath of a hurricane. They should thus be taken into account in order to correctly assess its overall impact.

Keywords: Hurricane, Ocean transport, Wave-current interactions

1. Introduction

The frequency of major tropical cyclones has increased in the past years (Bhatia et al., 2019; Kossin et al., 2020); however, estimating their impact on the coastal ocean circulation remains a challenge. Understanding wave-current interactions and representing their impact on coastal ocean transport processes is central to many coastal activities such as dredging, erosion management, oil and gas activities, search and rescue, and insurance (Bever and MacWilliams, 2013; Li and Johns, 1998; Breivik et al., 2013). All these activities require wave-current models to predict the impact of tropical cyclones on the coastal circulation and on water-level changes.

Wave-current interactions during a cyclone are highly nonlinear and vary significantly in space and time (Wu et al., 2011). Wave-induced currents are generated by wave radiation stress gradients (Longuet-Higgins, 1970), affecting water levels near shorelines and wave breaking points (Longuet-Higgins and Stewart, 1964). Changes in water levels and currents, in turn, affect the motion and evolution of the waves (Sikirić et al., 2013). Coupled wave-current models hence require the calculation of the full directional wave spectrum in order to correctly reproduce the dynamics of wind-driven surface waves. This is usually achieved by spectral wave models, which

20 describe the evolution of the wave energy spectrum. As of today, the most
21 popular spectral wave models are WAM (WAMDI Group, 1988), SWAN (Booij
22 et al., 1999), and WAVEWATCH III (Tolman et al., 2009). Among these
23 models, SWAN has been specifically developed for coastal applications, as
24 it represents depth-induced wave breaking and triad wave-wave interactions
25 using numerical techniques adapted to small-scale, shallow water regions
26 (Booij et al., 1999). However, WAVEWATCH III has recently been equipped
27 with new parallelization algorithm, domain decomposition and numerical
28 schemes for high resolution coastal applications (WW3DG, 2019; Abdolali
29 et al., 2020).

30 Coastal oceans are characterized by the complex topography of the coast-
31 line and the presence of islands, reefs and artificial structures. Traditional
32 structured-grid models lack the flexibility to simulate near-shore processes at
33 a sufficiently small scale. Although the use of nested structured grids allows
34 to locally refine the model resolution (Warner et al., 2010), staircase-like
35 representation of complex coastal topographies cannot be avoided. Instead,
36 unstructured-mesh models easily adapt to the topography and are hence
37 better suited to coastal processes (Fringer et al., 2019). Capturing the impact
38 of the topography on wave interactions becomes even more important in
39 the case of tropical cyclones. Heavy winds generate large wind-waves and
40 disturb ocean conditions (Liu et al., 2020) by causing coastal upwellings on
41 continental shelves (Smith, 1982) and inducing strong currents, waves and
42 storm surges in nearshore and coastal regions (Dietrich et al., 2010; Weisberg
43 and Zheng, 2006).

44 Ocean waves act as the dynamical interface between the atmosphere and
45 the ocean. Through this interface, tropical cyclones cause a cooling of the
46 upper ocean layer by vertical mixing and heat transfer (Aijaz et al., 2017;
47 Varlas et al., 2020). By altering the structure of the upper-ocean, hurricane
48 can cause the disruption of major ocean currents such as the Florida Current
49 and Gulf Stream (Oey et al., 2007). Interaction with hurricanes alters the

50 thermal structure of these currents as well as a significant decline of their
51 flow, resulting in delayed increased coastal levels along their path, even in
52 location out of reach of the hurricane itself (Ezer et al., 2017; Ezer, 2018).

53 Near the storm, heavy wind conditions also affect material transport at the
54 ocean surface. The transport of drifting objects or substances that are locally
55 released is often best represented by a Lagrangian individual-based model.
56 Such an approach is routinely used to model the dispersal of larvae, pollutants,
57 sediments and many other tracers (e.g. Le Hénaff et al., 2012; Liubartseva
58 et al., 2018; Figueiredo et al., 2013; Frys et al., 2020). Although some transport
59 model might take wave-induced currents into account, most of them neglect
60 wave-current interactions into account, which can lead to significant errors in
61 storm conditions (Röhrs et al., 2012; Curcic et al., 2016). Modeling studies
62 have investigated the impact of wave-current interactions during storm event
63 in lakes and inlets (Niu and Xia, 2017; Mao and Xia, 2018, 2020). However,
64 to our knowledge, there has been no similar study on the impact of hurricane-
65 induced wave-current interactions in coastal environments such as the Florida
66 Reef Tract (FRT), where transport processes might significantly impact the
67 biological connectivity.

68 The objective of this study is therefore to assess the importance of wave-
69 current interactions in the FRT during a tropical cyclone. We investigate
70 the transport of drifting particles on the Florida shelf during Hurricane Irma,
71 one of the strongest and costliest tropical cyclones on record in the Atlantic
72 Basin (Xian et al., 2018), which made landfall in Florida in September 2017.
73 To do that, we developed an unstructured-mesh coupled wave-current model
74 of South Florida to simulate the ocean circulation under hurricane conditions.
75 Both modeled currents and waves were validated against field measurements
76 and then used to simulate the transport of drifting material in the Florida
77 Keys and the Florida inner shelf. Model outputs were then compared with
78 uncoupled simulation results in order to assess the impact of wave-induced
79 forces and Stokes drift on the modeled currents and transports.

80 **2. Methods**

81 *2.1. Study area and observational data*

82 This study focuses on the South of Florida, as highlighted in Fig. 1.
83 The large-scale ocean circulation around South Florida is dominated by the
84 Florida Current (FC), which originates from the Loop Current (LC) where it
85 enters the Florida Straits from the Gulf of Mexico, and, downstream, forms
86 the Gulf Stream. The FC is a major western boundary current characterized
87 by spatial variability and meandering, associated with the presence of cyclonic
88 eddies between the core of the current and the complex reef topography of
89 the FRT (Lee et al., 1995; Kourafalou and Kang, 2012). The variability of
90 the FC extends over a large range of spatial and temporal scales, with periods
91 of 30-70 days in the Lower Keys (Lee et al., 1995) and shorter periods of
92 2-21 days in the Upper Keys (Lee and Mayer, 1977), and exhibits significant
93 seasonal and interannual cycles (Johns and Schott, 1987; Lee and Williams,
94 1988; Schott et al., 1988). Circulation on the West Florida Shelf (WFS), on
95 the other hand, is forced by local winds and tidal fluctuations (Lee and Smith,
96 2002; Liu and Weisberg, 2012). Furthermore, due to its location relative to
97 the warm waters of the North Atlantic, Florida is particularly vulnerable to
98 tropical cyclones. On average, the state gets hit by a hurricane every two
99 years and strong hurricanes, some of which are among the most destructive
100 on record, strike Florida on average once every four years (Malmstadt et al.,
101 2009).

102 The state of the ocean around Florida is monitored by an extensive
103 array of tide gauges, current meters and buoys. In this study, we used sea
104 surface elevation measurements from the National Oceanic and Atmospheric
105 Administrations (NOAA) Tides and Currents dataset. These measurements
106 were taken at four locations: two in the Florida Keys (Key West and Vaca
107 Key); one on the East coast of Florida (Virginia Key); and one on the West
108 coast (Naples). For the currents, we used ADCP measurements from the
109 University of South Florida's College of Marine Science's (USF/CMS) Coastal

110 Ocean Monitoring and Prediction System (COMPS) for the WFS (Weisberg
111 et al., 2009). More specifically, we used measurements from moorings C10,
112 C12 and C13, respectively located at the 25, 50, and 50 m isobaths of the
113 WFS (Liu et al., 2020). Finally, for the waves, we used measurements from
114 four buoys of the NOAA's National Data Buoy Center (NDBC); two on
115 Florida's eastern shelf and two on the WFS. The locations of all measurement
116 stations are shown in Fig. 1.

117 *2.2. Wind and atmospheric pressure during Hurricane Irma*

118 Hurricane Irma made landfall in Florida on 10 September 2017 as a
119 category 4 hurricane at Cudjoe Key (Florida Keys) and later as a category
120 3 hurricane on Marco Island, south of Naples (see hurricane track in Fig.
121 1). It then weakened to a category 2 hurricane as it moved further inland
122 (Cangialosi et al., 2018). The storm damaged up to 75% of the buildings
123 at its landfall point in the Florida Keys, making it one of the strongest and
124 costliest hurricanes on record in the Atlantic basin (Xian et al., 2018; Zhang
125 et al., 2019). The strongest reported sustained winds on Marco Island was
126 50 m/s while the highest recorded storm surge was 2.3 m, although larger
127 wind speed likely occurred in the Florida Keys (Pinelli et al., 2018). To
128 reproduce the wind profile of Irma in our model, we used high-resolution
129 H*Wind wind fields (Powell et al., 1998). As these data represent 1-min
130 averaged wind speeds, we multiplied them by a factor 0.93 to obtain 10-min
131 averaged wind speeds (Harper et al., 2010). This conversion factor accounts
132 for the greater variance of mean winds measured over periods shorter than
133 10 minutes, therefore producing more erratic value. Furthermore, H*Wind
134 wind profiles did not cover the whole model extent during the passage of the
135 hurricane and were thus blended within coarser wind field extracted from
136 ECMWF ERA-5 datasets (Fig. 2A). The pressure field during the passage
137 of Hurricane Irma was also reconstructed using ERA-5 data. However, the
138 coarse resolution of the dataset smoothes out the depression at the center of
139 the hurricane, leading to an underestimation of the pressure gradient (Fig.

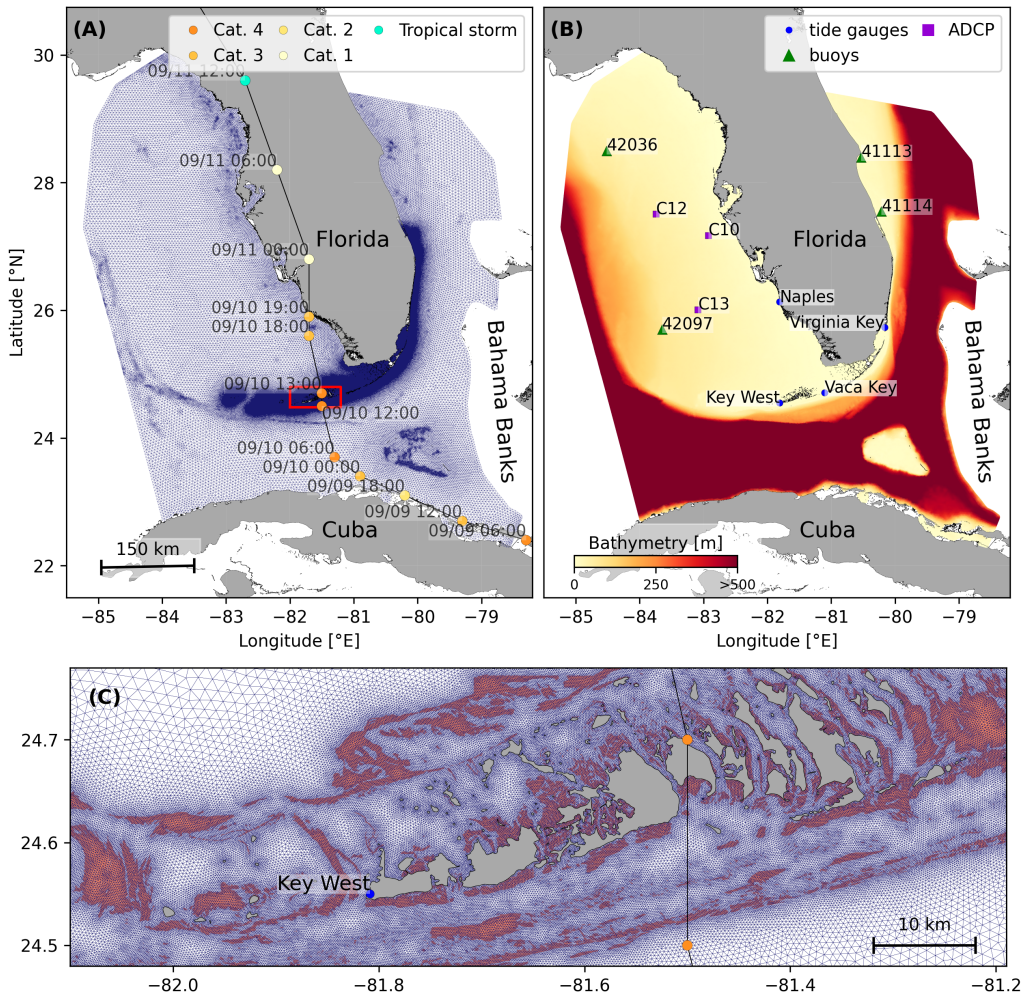


Fig. 1: (A) Mesh of the computational domain with the trajectory of Irma. The category of the hurricane is given by the Saffir-Simpson color scale. (B) Bathymetry of the domain with the location of stations used for the validation of the model outputs. (C) Close up view of the Lower Keys area (red squares in (A)), where the mesh resolution reaches 100 m near reefs (shown in dark orange) and islands (highlighted in dark grey)

140 2B). To better capture the central depression of Irma, we therefore built a
 141 hybrid pressure field using the position and the minimal pressure of the core
 142 of the hurricane based on its track as recorded in the HURDAT 2 database
 143 (Landsea and Franklin, 2013). Based on this information, the hybrid pressure
 144 field was constructed by combining an idealized Holland pressure profile (Lin
 145 and Chavas, 2012) within the radius of maximum wind speed of Irma (Knaff
 146 et al., 2018) with ERA-5 pressure field. The transition from the Holland
 147 profile to ERA-5 data outside the radius of maximum wind speed data was
 148 performed using a smooth step function (Fig. 2).

149 *2.3. Hydrodynamic model*

150 Ocean currents generated during hurricane Irma around South Florida
 151 were modeled using the 2D barotropic version of the unstructured-mesh
 152 coastal ocean model SLIM¹ (Lambrechts et al., 2008). The model mesh covers
 153 an area similar to the model extent of Dobbelaere et al. (2020), that includes
 154 the FRT but also the Florida Straits and part of the Gulf of Mexico (Figure 1).
 155 However, this area has been slightly extended northeastward and westward
 156 in order to include the NOAA-NDBC buoys. Furthermore, to withstand
 157 potential cell drying during the hurricane, we solved the conservative shallow
 158 water equations with wetting-drying:

$$\begin{aligned}
 \frac{\partial H}{\partial t} + \nabla \cdot (\mathbf{U}) &= 0 , \\
 \frac{\partial \mathbf{U}}{\partial t} + \nabla \cdot \left(\frac{\mathbf{U}\mathbf{U}}{H} \right) + f\mathbf{e}_z \times \mathbf{U} &= \alpha g H \nabla(H - h) - \frac{1}{\rho} \nabla p_{\text{atm}} + \frac{1}{\rho} \boldsymbol{\tau}_s \\
 &\quad + \nabla \cdot (\nu \nabla \mathbf{U}) - \frac{C_b}{H^2} |\mathbf{U}| \mathbf{U} + \gamma (\mathbf{U}_{\text{ref}} - \mathbf{U}) ,
 \end{aligned} \tag{1}$$

159 where H is the water column height and \mathbf{U} is the depth-averaged transport;
 160 f is the Coriolis coefficient; g is the gravitational acceleration; h is the

¹<https://www.slim-ocean.be>

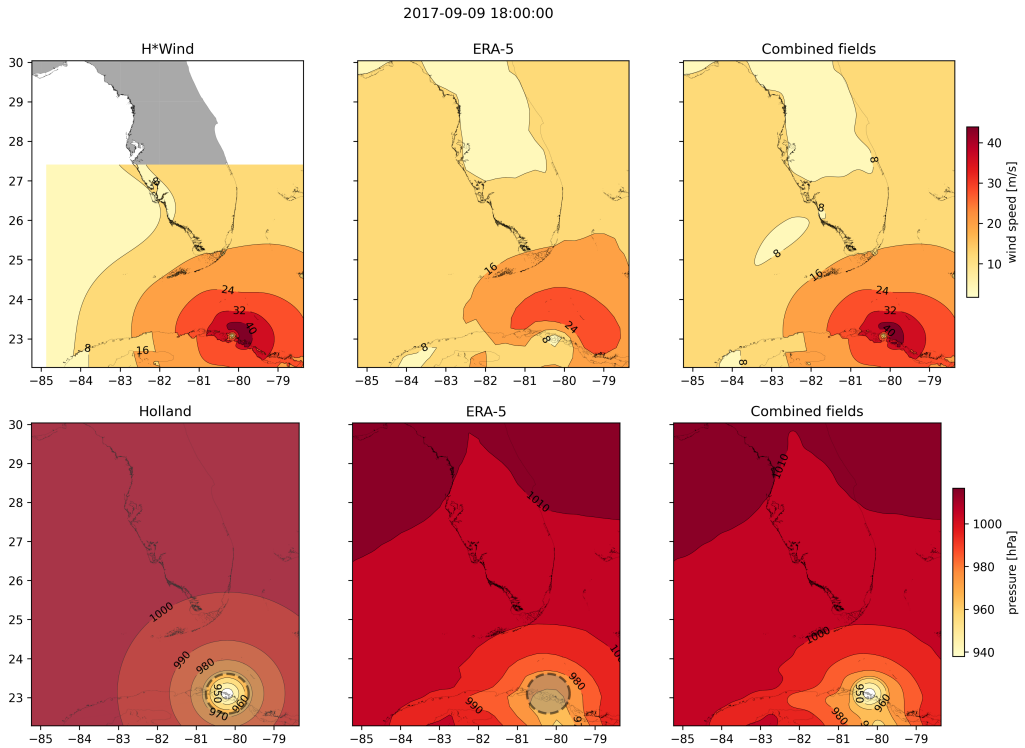


Fig. 2: Snapshot of the hybrid wind (top) and pressure (bottom) profiles constructed to capture the passage of Hurricane Irma at 1800 UTC on 9 September 2017. Wind profiles are obtained by combining high resolution H*Wind with coarser ERA-5 wind fields. The pressure field is built by combining the ERA-5 pressure field with an idealized Holland pressure profile based on the track of Irma in the HURDAT 2 database. Holland field was only used within the radius of maximum wind speed (dashed grey line) of the hurricane to capture its central depression.

161 bathymetry; α is a coefficient indicating whether the mesh element is wet
 162 ($\alpha = 1$) or dry ($\alpha = 0$) (Le et al., 2020); ν is the viscosity; C_b is the bulk
 163 bottom drag coefficient; p_{atm} is the atmospheric pressure; τ_s is the surface
 164 stress, usually due to wind; and γ is a relaxation coefficient towards a reference
 165 transport \mathbf{U}_{ref} . As this study focuses on transport processes and not coastal
 166 flooding, wetting-drying is only applied on wet grid cells that may become dry
 167 under the influence of the hurricane. As in Frys et al. (2020) and Dobbelaere
 168 et al. (2020), SLIM currents were gradually relaxed towards the operational
 169 Navy HYCOM product (GOMl0.04², Chassignet et al. (2007)) in regions where
 170 the water depth exceeds 50 m. HYCOM's 3D currents were depth-integrated
 171 into 2D transports to be used as forcing in the model. Moreover, these
 172 transports as well as HYCOM's sea surface elevation were used as boundary
 173 condition in the model.

174 We adapted the parameterization of the wind-induced surface stress to
 175 storm conditions. At very high wind speeds, the white cap is blown off
 176 the crest of the waves. This phenomenon, also known as spume, has been
 177 hypothesized to generate a layer of droplets that acts as a slip layer for the
 178 winds at the ocean-atmosphere interface (Holthuijsen et al., 2012). It causes
 179 a saturation of the wind drag coefficient for strong winds (Powell et al., 2003;
 180 Donelan et al., 2004; Curcic and Haus, 2020). We take this saturation effect
 181 into account by using the wind drag parameterization of Moon et al. (2007).
 182 In this parameterization, the drag coefficient C_d depends on the wind speed
 183 at 10-m height U_{10} according to:

$$C_d = \kappa^2 \log \left(\frac{10}{z_0} \right)^{-2} \quad (2)$$

184 where κ is the von Karman constant and z_0 is the roughness length expressed

²<https://www.hycom.org/data/goml0pt04>

185 as:

$$z_0 = \begin{cases} \frac{0.0185}{g} u_*^2 & \text{if } U_{10} \leq 12.5 \text{ m/s ,} \\ [0.085(-0.56u_*^2 + 20.255u_*) + 2.458] - 0.58] \times 10^{-3} & \text{if } U_{10} > 12.5 \text{ m/s ,} \end{cases} \quad (3)$$

186 with u_* the friction velocity. The relation between U_{10} and u_* is given by:

$$U_{10} = -0.56u_*^2 + 20.255u_* + 2.458 . \quad (4)$$

187 The mesh resolution depends on the distance to the coastlines and reefs
188 following the approach of Dobbelaere et al. (2020). The mesh is then further
189 refined according to bathymetry value and gradient, as suggested in the
190 SWAN user-guide³. Such an approach improves the model efficiency as the
191 mesh resolution is only increased where required by the currents and waves
192 dynamics. The mesh was generated with the seamsh⁴ Python library, which is
193 based on the open-source mesh generator GMSH (Geuzaine and Remacle,
194 2009). It is composed of approximately 7.7×10^5 elements. The coarsest
195 elements, far away from the FRT, have a characteristic length of about 5 km
196 whereas the finest elements have a characteristic length of about 100 m along
197 the coastlines and over the reefs (Fig 1).

198 *2.4. Wave model*

199 Waves were modeled using the parallel unstructured-mesh version of the
200 Simulating WAves Nearshore (SWAN) model (Booij et al., 1999), one of the
201 most popular wave models for coastal areas and inland waters. It solves the
202 action balance equation (Mei, 1989):

$$\frac{\partial N}{\partial t} + \nabla_{\mathbf{x}} \cdot [(\mathbf{c}_g + \mathbf{u})N] + \frac{\partial}{\partial \theta}[c_\theta N] + \frac{\partial}{\partial \sigma}[c_\sigma N] = \frac{S_{in} + S_{ds} + S_{nl}}{\sigma} , \quad (5)$$

³<http://swanmodel.sourceforge.net/unswan/unswan.htm>

⁴<https://pypi.org/project/seamsh/>

203 where $N = E/\sigma$ is the wave action density and E is the wave energy spectrum;
204 θ is the wave propagation direction; σ is the intrinsic wave frequency; \mathbf{c}_g is
205 the wave group velocity, $\mathbf{u} = \mathbf{U}/H$ is SLIM depth-averaged current velocity;
206 c_θ and c_σ are the propagation velocities in spectral space due to refraction
207 and shifting in frequency due to variations in depth and currents; and S_{in} ,
208 S_{ds} , and S_{nl} respectively represent wave growth by wind, wave decay and
209 nonlinear transfers of wave energy through four and three-wave interactions,
210 *i.e.* quadruplets and triplets. The wave spectra were discretized with 48
211 direction bins and 50 frequency bins logarithmically distributed from 0.03 to
212 2 Hz. Exponential wind growth was parameterized using the formulation of
213 Janssen (1991), while dissipations by whitecapping and bottom dissipation
214 followed the formulations of Komen et al. (1984) and Madsen et al. (1989),
215 respectively.

216 Coefficients for exponential wind growth and whitecapping parameteriza-
217 tions were based on the results of Siadatmousavi et al. (2011), and significantly
218 differ from SWAN’s default settings. By default, SWAN implements the wind
219 input formulation of Komen et al. (1984) and the steepness-dependent co-
220 efficient governing dissipation by whitecapping is a linear function of the
221 wavenumber. In this study, this steepness-dependent coefficient is a quadratic
222 function of the wavenumber, as it showed better predictions of the significant
223 wave height in the study of Siadatmousavi et al. (2011). The choice of these
224 formulations was motivated by the appearance of numerical instabilities in
225 the region of the Gulf Stream when using SWAN’s default parameter values.
226 Finally, ERA5 wave spectra was used as boundary condition in the model.
227 Wave spectra is obtained from the ocean wave model WAM and is given on a
228 $1^\circ \times 1^\circ$ grid with 24 directions and 36 frequencies.

229 Surface waves induce a net drift in the direction of the wave propagation,
230 known as the Stokes drift (Van Den Bremer and Breivik, 2018; Stokes,
231 1880). This net drift has a significant impact on sediment transport in
232 nearshore regions (Hoefel and Elgar, 2003), on the formation of Langmuir

233 cells (Langmuir, 1938; Craik and Leibovich, 1976) as well as on the transport
 234 of heat, salt or pollutants such as oil or micro-plastic in the upper ocean layer
 235 (McWilliams and Sullivan, 2000; Röhrs et al., 2012; Drivdal et al., 2014). To
 236 correctly model the Stokes drift profile in mixed wind-driven sea and swell
 237 conditions, the full two-dimensional wave spectrum must be represented by a
 238 spectral wave model within a wave-current coupling (Van Den Bremer and
 239 Breivik, 2018). We therefore used SWAN modeled spectra to compute the
 240 Stokes drift as follows:

$$\mathbf{u}_s = \int_0^{2\pi} \int_0^{+\infty} \frac{\sigma^3}{h \tanh(2kh)} E(\sigma, \theta) (\cos \theta, \sin \theta) d\sigma d\theta , \quad (6)$$

241 where k is the norm of the wave vector; h is the water depth; and $E(\sigma, \theta)$ is
 242 the wave energy density.

243 *2.5. Coupled model*

244 SLIM and SWAN are coupled so that they run on the same computational
 245 core and the same unstructured mesh. SLIM is run first and passes the
 246 wind velocity (\mathbf{U}_{10}), water level ($\eta = H - h$) and depth-averaged current
 247 ($\mathbf{u} = \mathbf{U}/H$) fields to SWAN, as well as a roughness length (z_0) for the bottom
 248 dissipation formulation of Madsen et al. (1989). This roughness length is
 249 computed from SLIM's bulk drag coefficient C_b following the approach of
 250 Dietrich et al. (2011) so that both models have consistent bottom dissipation
 251 parameterizations. SWAN then uses these quantities to compute the wave
 252 radiation stress gradient, that is then passed to SLIM as the force exerted
 253 by waves on currents $\boldsymbol{\tau}_{\text{wave}}$ (Fig. 3). SLIM then uses this quantity to
 254 update the value of the surface stress $\boldsymbol{\tau}_s$ in Eq. (1), that now becomes
 255 the sum of wind and wave-induced stresses $\boldsymbol{\tau}_s = \boldsymbol{\tau}_{\text{wind}} + \boldsymbol{\tau}_{\text{wave}}$. Here, the
 256 momentum flux from the atmosphere to the ocean is taken as the commonly-
 257 used full wind stress $\boldsymbol{\tau}_{\text{wind}}$. Doing so, we neglect the momentum advected
 258 away from the storm by the waves, leading to a 10-15% overestimation of the
 259 momentum flux in hurricane winds (Curcic, 2015). Moreover, we followed

260 the approach of Dietrich et al. (2012) by characterizing the wave-induced
261 stresses using the radiation-stress representation instead of the vortex-force
262 representation (McWilliams et al., 2004). Although the latter provides a
263 clearer and more meaningful decomposition of the wave effect, we implemented
264 the first representation for the sake of simplicity as it allows us to provide
265 the whole wave contribution as an additional surface stress to SLIM (Lane
266 et al., 2007).

267 [Talk a bit more about difference between VF and RS]

268 SLIM's governing equations are integrated using an implicit time integration
269 scheme while SWAN is unconditionally stable (Dietrich et al., 2012),
270 allowing both models to be run with relatively large time steps. In this study,
271 the stationary version of SWAN was used, *i.e.* the first term of Eq. (5) was
272 set to zero. This resulted in reduced scaling and convergence rates than with
273 the nonstationary version of SWAN but increased the stability of the model.
274 The wave spectra at each node of the mesh was saved at the end of each
275 iteration to serve as initial conditions for the next one. Both models were
276 run sequentially using a time step of 600 s, so that each computational core
277 was alternatively running either SLIM or SWAN. As in the coupling between
278 SWAN and ADCIRC (Dietrich et al., 2012), both models use the same local
279 sub-mesh, allowing for a one-to-one correspondence between the geographic
280 locations of the mesh vertices. No interpolation is therefore needed when
281 passing the discretised variables from one model to the other, which allows
282 an efficient inter-model communication. However, as SLIM is based on a
283 discontinuous Galerkin finite element method, an additional conversion step
284 to a continuous framework was required to transfer SLIM nodal quantities to
285 SWAN.

286 *2.6. Quantifying the effect of wave-current interactions on transport*

287 To quantify the impact of wave-current interactions on transport processes,
288 we compared the trajectories of passive particles advected by the uncoupled
289 SLIM and coupled SLIM+SWAN currents during the passage of Irma in the

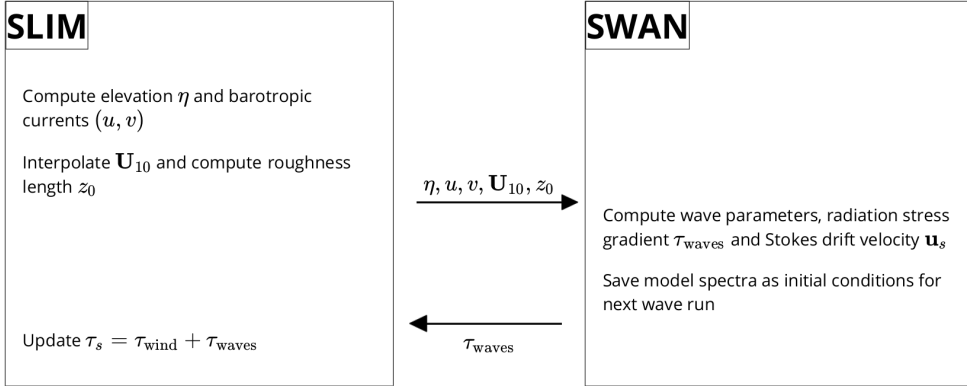


Fig. 3: Schematic illustration of the coupled SLIM+SWAN model.

290 Lower Keys. Furthermore, the depth-averaged Stokes drift was computed
 291 using the wave spectra of the coupled model SLIM+SWAN run as well as
 292 those of an uncoupled SWAN run. Particles were released on the inner and
 293 outer shelves at the points highlighted by red and blue dots in Fig. 4 on
 294 Sept. 7 at 0000 UTC and then tracked until Sept. 15. These initial particle
 295 positions were found using backtracking methods (Spivakovskaya et al., 2005)
 296 to ensure that the release particles would intersect the path of Irma during
 297 its passage through the Florida Keys. We first defined two 25 km^2 circular
 298 regions on the trajectory of the hurricane (see red and blue circles in Fig. 4).
 299 Particles within these two regions were then tracked backward in time using
 300 uncoupled SLIM currents from the exact time of the passage of the hurricane
 301 until Sept. 7 at 0000 UTC. Their positions at the end of the backward
 302 simulation (see red and blue particle clouds in Fig. 4) corresponds to the
 303 initial condition of the forward transport simulations described below. We
 304 then compared the trajectories of particles originating from these regions and
 305 advected forward in time by different sets of currents: (i) uncoupled SLIM
 306 currents alone; (ii) coupled SLIM+SWAN currents; (iii) SLIM currents with
 307 the addition of the depth-averaged Stokes drift computed with the coupled
 308 wave-current model (Stokes-C); (iv) SLIM+SWAN currents with Stokes-C;

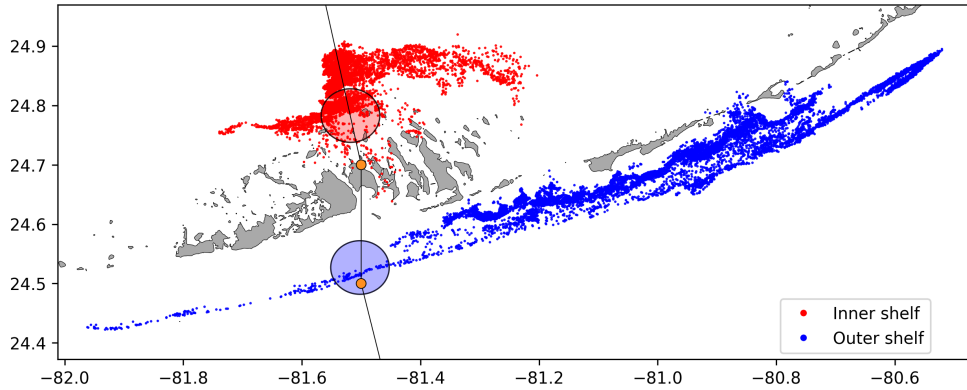


Fig. 4: Release regions of the passive particles on the inner and outer shelves (red and blue clouds) obtained by backtracking particles released in the red and blue circular areas during the passage of Irma.

and (v) SLIM currents with the depth-averaged Stokes drift computed with the uncoupled wave model (Stokes-U). The different combinations of Eulerian currents and Stokes drifts used to model the transport of passive drifters in the Lower Keys on the passage of Hurricane Irma are summarized in Table 1. Particle trajectories are compared by computing the distances between the centers of mass of the particle clouds through time.

3. Results

We first validated the reconstructed atmospheric fields of hurricane Irma as well as the outputs of our coupled wave-current model against field measurements. We then used the validated model outputs to simulate the transport of passive particles in the Lower Keys during the passage of Hurricane Irma. These particles were advected by the sets of currents described in section 2.6 and their trajectories were compared to evaluate the impact of the wave-current interactions and the Stokes drift on the transport processes during the passage of Irma.

Name	Physics
SLIM	Eulerian currents from uncoupled SLIM simulation
SLIM+SWAN	Eulerian currents impacted by RS gradient from coupled SLIM+SWAN simulation
SLIM+Stokes-U	Eulerian currents from uncoupled SLIM run with Stokes drift from uncoupled SWAN simulation
SLIM+Stokes-C	Eulerian currents from uncoupled SLIM run with Stokes drift from coupled SLIM+SWAN simulation
SLIM+SWAN+Stokes-C	Eulerian currents impacted by RS gradient and Stokes drift from coupled SLIM+SWAN simulation

Table 1: Summary of the different combinations of Eulerian currents and Stokes drifts used to model the transport of passive drifters on the passage of Hurricane Irma in the Lower Keys

324 *3.1. Model validation*

325 H*Wind winds and hybrid pressure field agree well with station mea-
 326 surements at Vaca Key station (Fig. 5). The hybrid pressure field shows a
 327 better agreement with observations than ERA-5 pressure as it successfully
 328 reproduces the storm depression. ERA-5 fields, on the other hand, fail to
 329 reproduce the low pressure at the core of the hurricane due to their coarser
 330 grid, leading to an overestimation of 8 mbar of the storm depression. Both
 331 H*Wind and ERA-5 agree well with observed wind speeds although both
 332 data sets tend to slightly overestimate the width and intensity of the wind
 333 peak. However, H*Wind profiles better reproduce the timing of the observed
 334 peak, as ERA-5 winds tend to anticipate it. H*wind also exhibits a slightly
 335 narrower peak in wind speed, which better agrees with observations.

336 Hydrodynamic outputs of the coupled wave-current model agree well
 337 with tide gauge (Fig. 6) and ADCP measurements (Fig. 7). Despite a
 338 slight overestimation of the amplitude of sea surface elevation in fair weather

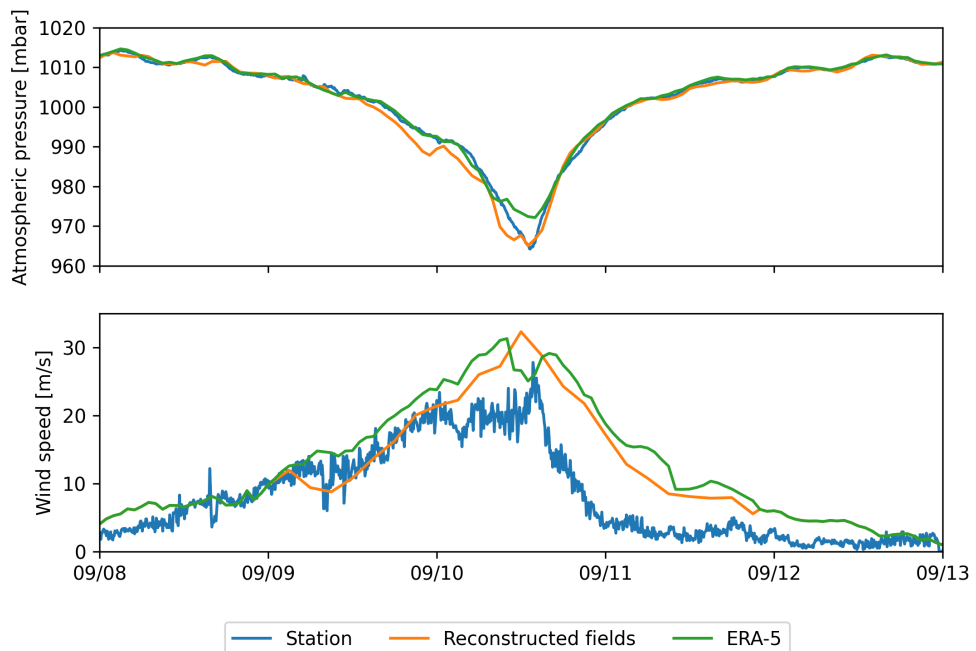


Fig. 5: Comparison of reconstructed wind (top) and atmospheric pressure (bottom) with field measurements and coarser ECMWF ERA-5 profiles at Vaca Key station. The generated hybrid atmospheric forcings better reproduce the observed storm depression while H*wind winds better reproduce the measured peak in wind speed.

339 conditions, the timing and amplitude of the storm surges are well reproduced
340 by the coupled model. The largest model error during the surge is an
341 overestimation of 18 cm of the elevation peak at Virginia Key. The fit is
342 especially good at Naples, where both the large positive and negative surges
343 are captured by the coupled model with an error of less than 5 cm. Modeled
344 2D currents were validated against depth-averaged ADCP measurements
345 at mooring stations C10 (Fig. 7), C12 and C13. As in Liu et al. (2020),
346 we performed the vector correlation analysis of Kundu (1976) to compare
347 modeled and observed current velocity vectors. Correlation coefficients (ρ)
348 between simulated and observed depth-averaged currents are 0.84, 0.74 and
349 0.73 at stations C10, C12 and C13, respectively. The average veering angles
350 are below 12°, as in (Liu et al., 2020). Furthermore, the positive bias in Table
351 2 indicates that our model tends to underestimate the southward component
352 of the currents at the different stations. As expected from a depth-averaged
353 model, the best fit with observations is obtained at the shallowest mooring
354 C10, located on the 25 m isobath, with an average veering angle of 6° and
355 smaller error statistics (Table 2).

356 The simulated significant wave height agrees well with observations on the
357 WFS (buoys 41113 and 41114), where errors on the peak value do not exceed
358 5% (Fig. 8). On Florida's eastern shelf (buoys 42036 and 42097), errors
359 are slightly larger and reach 20%. Although the model outputs agree well
360 with observations, a lag in significant wave height is observed for all 4 buoys.
361 Moreover, the peak in significant wave height tends to be underestimated at
362 buoys 41113 and 41114, located on the eastern shelf of Florida. The same
363 tendency is observed with the modeled wave period, with mean errors inferior
364 to 1 second on the WFS and reaching more than 2 seconds on Florida's
365 eastern shelf (Table 2), as the coupled model fails to reproduce the observed
366 peak in wave period between the 7th and 8th of September on this side of
367 Florida. Finally, modeled wave direction agrees well with observation (Fig. 8),
368 although our model tends to overestimate wave propagation in the northward

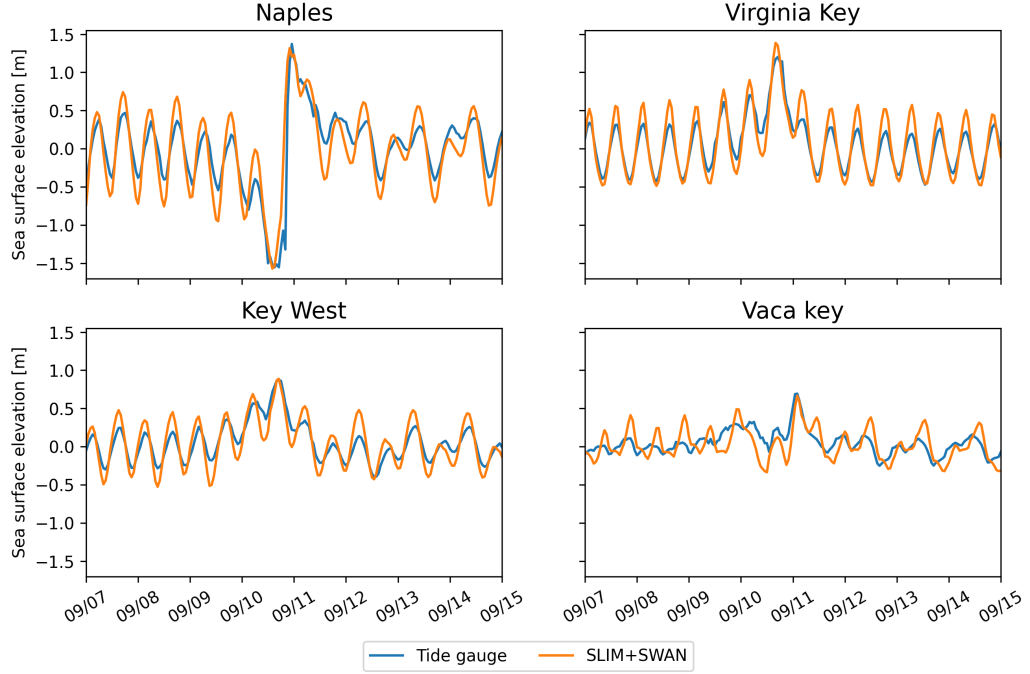


Fig. 6: Comparison of modeled sea surface elevation at the 4 tide gauges shown in Fig. 1B. The timing and amplitude of the storm surges are well reproduced by the model

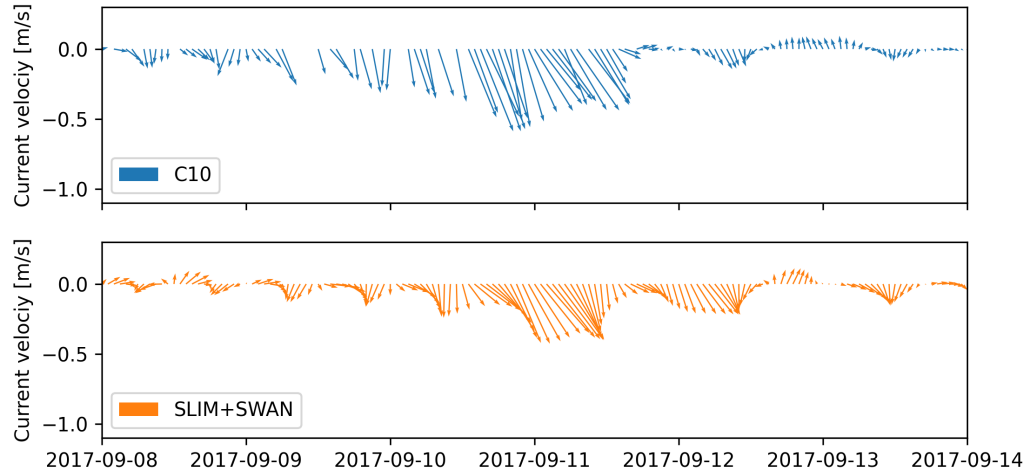


Fig. 7: Comparison of modeled current velocity with observed velocity at mooring C10 (see Fig. 1B for its location). Modeled current velocities agree well with observations, with a correlation coefficient of 0.84 and an average veering angle of 6° .

369 direction at stations 41114 and 41113 on the passage of the hurricane (not
370 shown).

371 *3.2. Impact of waves on currents and transport*

372 We evaluated the impact of wave-current interactions on modeled currents
373 during the passage of Irma in the Lower Keys, between Sept. 7 and 13, 2017.
374 First, we computed the maximum difference between currents modeled by
375 SLIM and SLIM+SWAN during this period (Fig. 9A). The largest differences
376 in current speed were observed over the reefs, on the shelf break and around
377 islands. They locally reach 1 m/s, with the coupled SLIM+SWAN model
378 yielding the largest amplitudes. The regions where the differences are the
379 largest experience the strongest radiation-stress gradient τ_{wave} (Fig. 9B)
380 induced by wave energy dissipation on the shelf-break and rough seabed
381 induce variations of the wave radiation stress (Longuet-Higgins and Stewart,
382 1964). This highlights the important protective role of the barrier formed
383 by the offshore reefs, that require a fine spatial resolution to be accurately
384 captured. Wave-induced differences in current speed were amplified by the
385 action of the wind stress τ_{wind} (Fig. 9C). Wind speeds were larger in the front
386 right quadrant of the hurricane (Zedler et al., 2009), yielding larger differences
387 on the right-hand side of the storm trajectory. This is especially clear in the
388 area between the Florida Keys and the Everglades, where relatively small
389 values of τ_{wave} nonetheless produce current speed differences of up to 0.5 m/s
390 because of the wind stress.

391 Waves play a significant role on the transport processes during and after the
392 passage of hurricane Irma (Fig. 10A,B). Comparing SLIM and SLIM+SWAN
393 shows that wave-current interactions alone yield differences of up to 5 km
394 between the modeled trajectories on the passage of the hurricane. These
395 differences exceed 10 km on the outer shelf when Stokes drift is taken into
396 account. Such deflections are not negligible when compared to the total
397 distance traveled by particle clouds. For all simulations, modeled particles
398 were transported up to 30 km from their release point on the inner shelf

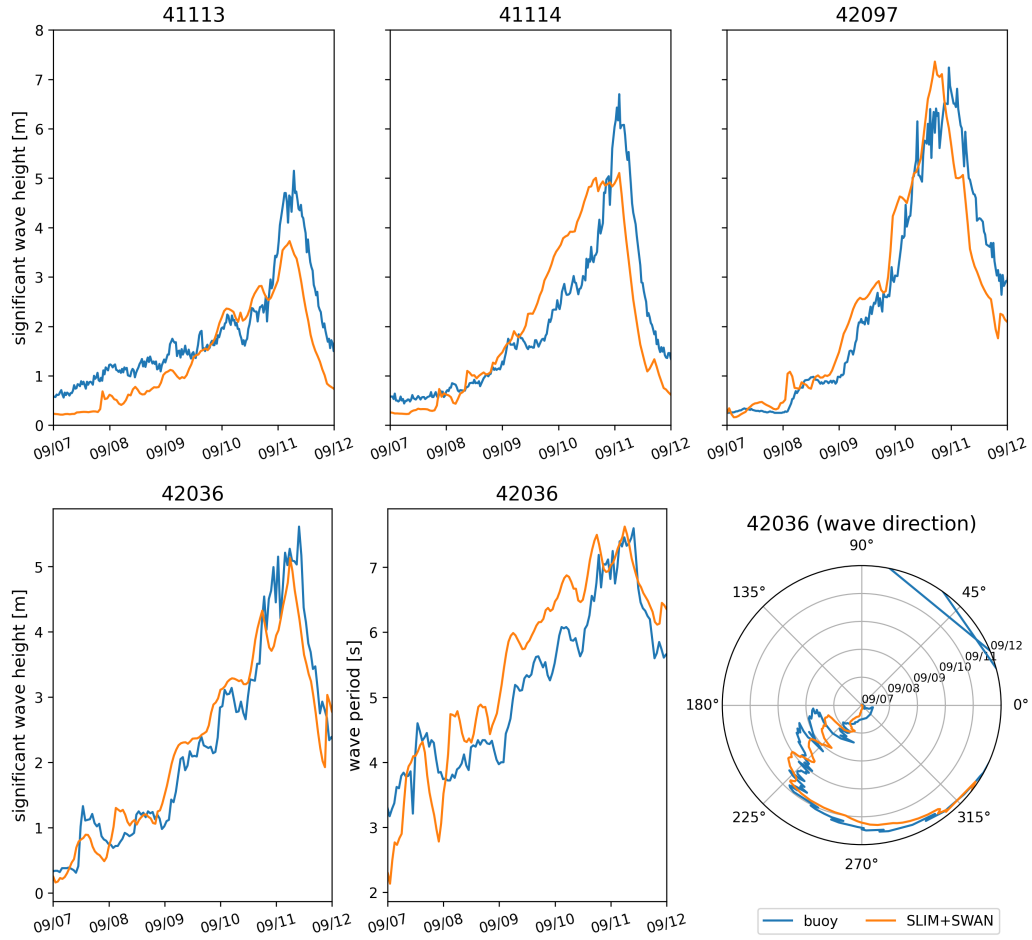


Fig. 8: Comparison of modeled wave parameters with observation at the 4 buoys location (locations shown in Fig. 1B). The modeled significant wave heights agree well with field measurement.

Station	Variable	Bias	MAE	RMSE
Vaca Key	sse (m)	n/a	0.12	0.16
	U_{10} (m/s)	1.51	1.85	2.61
	p_{atm} (hPa)	-0.21	0.59	1.03
Key West	sse (m)	n/a	0.11	0.13
Virginia Key	sse (m)	n/a	0.10	0.13
Naples	sse (m)	n/a	0.18	0.23
C10	u (m/s)	-0.006	0.04	0.05
	v (m/s)	0.02	0.06	0.08
C12	u (m/s)	-0.01	0.06	0.07
	v (m/s)	0.06	0.09	0.11
C13	u (m/s)	0.004	0.06	0.08
	v (m/s)	0.04	0.06	0.08
41113	H_s (m)	-0.35	0.40	0.51
	T_m (s)	-2.18	2.47	3.13
	θ_m (degree)	7.17	19.50	26.06
41114	H_s (m)	-0.21	0.53	0.68
	T_m (s)	-1.69	2.53	3.15
	θ_m (degree)	31.25	35.28	46.18
42036	H_s (m)	-0.03	0.26	0.36
	T_m (s)	0.04	0.65	0.77
	θ_m (degree)	19.92	30.65	41.69
42097	H_s (m)	-0.15	0.40	0.57
	T_m (s)	0.02	0.62	0.74
	θ_m (degree)	3.62	28.08	45.89

Table 2: Error statistics on the wave-current model outputs as compared to the measured sea surface elevation (sse), eastward and northward depth-average current velocities (u,v), significant wave height (H_s), zero-crossing mean wave period (T_m) and mean wave direction (θ_m). Model bias, mean absolute error (MAE), and root mean squared error (RMSE) are listed by variable (unit) and value.

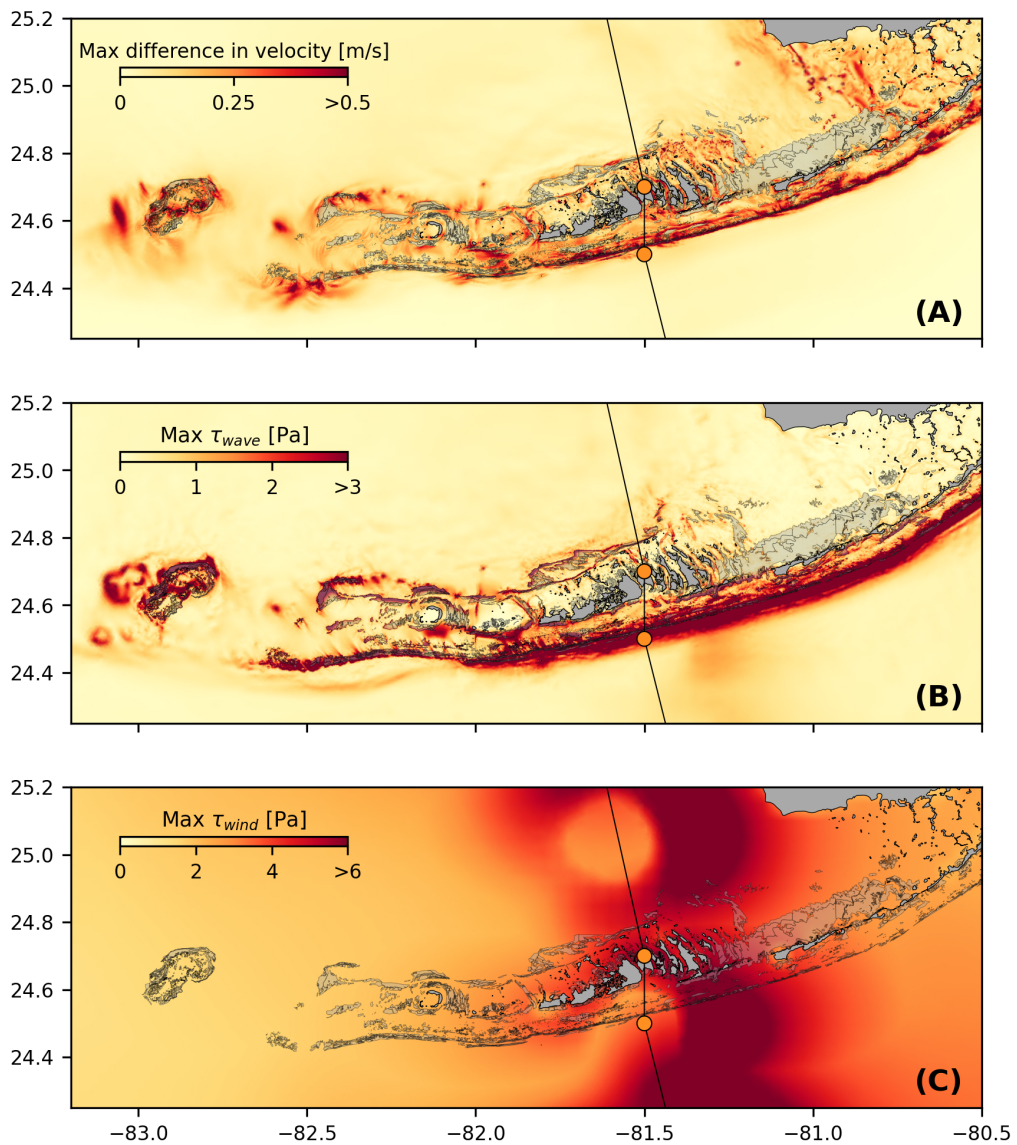


Fig. 9: (A). Maximum difference between SLIM and SLIM+SWAN currents during the passage of Irma in the Lower Florida Keys; (B) Maximum wave radiation stress gradient τ_{wave} and (C) maximum wind stress τ_{wind} (C) generated by the hurricane. Radiation stress gradient yields difference larger than 0.5 m/s (and locally reaching 1m/s) in current velocities, especially over offshore reefs.

399 and up to 60 km on the outer shelf. The impact of the waves on the
400 transport processes differs significantly between the inner and outer shelves,
401 with wave-induced differences in trajectories 4 to 5 times larger on the outer
402 shelf. Furthermore, the distance between the centers of mass of the clouds
403 of particles tends to stabilize on the inner shelf after the passage of Irma,
404 while it keeps increasing on the outer shelf up to two days after the passage
405 of the hurricane when taking Stokes drift into account. The distance then
406 stabilizes for about a day before it starts decreasing (see right panel of Fig.
407 10A,B). However, when considering wave-current interactions alone (SLIM
408 vs. SLIM+SWAN), the distance between the clouds of particles starts to
409 decrease just after the passage of Irma.

410 The Stokes drift appears to have a larger effect than the radiation stress
411 gradient and the wave-current interactions (Fig 10A,B). Nonetheless, compar-
412 ing the different curves for the outer shelf suggests that the radiation-stress
413 gradient induces effects similar to the impact of the Stokes drift in this
414 region during the passage of Irma. However, when comparing SLIM and
415 SLIM+SWAN both on the inner and outer shelf, this impact appears to be
416 negligible during the rest of the simulation. Comparing Stokes-U and Stokes-C
417 indicates that the difference between the trajectories of particles advected by
418 the two Stokes drifts does not exceed 2 km, with larger discrepancies on the
419 outer shelf (Fig. 10C,D). The distance between the two clouds of particles
420 increases abruptly on the passage of the hurricane (and two days after on the
421 outer shelf) and then stabilizes during the rest of the simulation.

422 4. Discussion

423 The coupled SLIM+SWAN model correctly reproduces the hydrodynamics
424 and wave dynamics during hurricane Irma. Such good agreement with field
425 measurements can only be achieved using accurate forcings and adequate
426 wave parameterizations. By comparing coupled and uncoupled model runs, we
427 showed that neglecting wave radiation stress gradient can induce differences

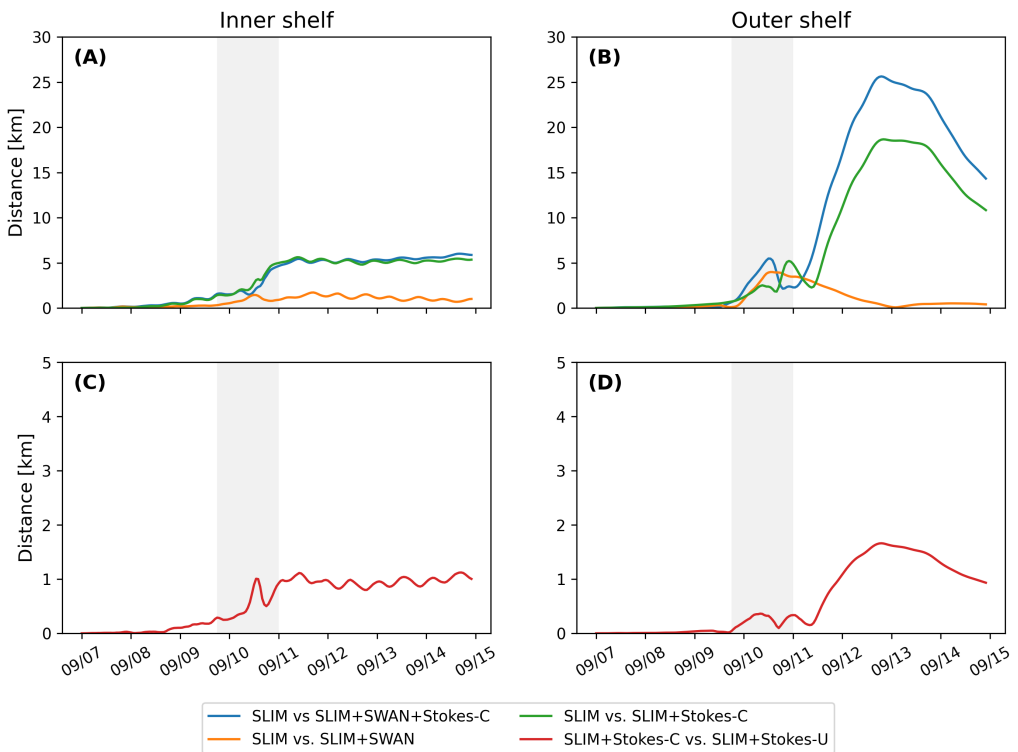


Fig. 10: Difference between the centers of mass of the particle clouds released from the regions highlighted in Fig. 4 and advected by different combinations of coupled and uncoupled velocity fields.

428 of up to 1 m/s in modeled current velocities. The radiation stress gradient
429 during the hurricane was especially large over the shelf break, where waves
430 are strongly dissipated by the offshore coral reef barrier. The radiation stress
431 gradient alone can deflect drifting particles by up to 5 km during the passage
432 of the hurricane. These differences in modeled trajectories were significantly
433 larger and required more time to stabilize on the outer shelf. The impact of
434 the Stokes drift dominates the effects of wave-current interactions through the
435 radiation stress gradient, except during the passage of the hurricane, when
436 both contributions are similar. Finally, neglecting wave-current interactions
437 when computing Stokes drift leads to variations of up to 2 km in modeled
438 trajectories on the passage of the hurricane.

439 Despite slightly overestimating the amplitude of the sea surface elevation in
440 fair weather conditions, the coupled wave-current model correctly reproduces
441 the timing and amplitude of the observed storm surge. All elevation peaks are
442 captured with a 4% accuracy at every station except Virginia key, where the
443 surge was overestimated by about 15%. Such accuracy is key to predict the
444 damages caused by the hurricane, as most destroyed and severely damaged
445 buildings in the Florida Keys during Hurricane Irma were caused by storm
446 surge and waves (Xian et al., 2018). Furthermore, by using a high-resolution
447 model, we can explicitly reproduce the circulation between all the reefs and
448 islands of the Florida Keys. The fine-scale details of the storm surge, and
449 hence the associated risk, are thus accurately represented. In addition to
450 accurately capturing positive surges, the model also reproduced the observed
451 negative surge in Naples with an error of about 1%. This result is of interest
452 from a biological point of view as negative surges, although less studied, affect
453 water exchanges between the estuaries and the coastal ocean and disturb
454 the benthic ecosystems (Liu et al., 2020). Such rapid decrease in water
455 level followed by a positive surge cause massive freshwater inflows, causing a
456 significant decrease in water salinity (Wachnicka et al., 2019).

457 Strong currents such as the Gulf Stream affect waves trough refraction

458 over gradients in current velocity, shoaling and breaking of opposing waves or
459 lengthening of following waves (Hegermiller et al., 2019). Under hurricane
460 conditions, these interactions can cause numerical instabilities in the wave
461 model if the parameterizations are not appropriate and the model resolution
462 not sufficient. Hegermiller et al. (2019), for instance, used a 5-km model
463 grid and 48 directional bins to capture spatial gradients in wave height
464 induced by wave-currents interactions in the Gulf Stream during Hurricane
465 Matthew (2016). We followed these guidelines when defining the coarsest
466 resolution of the model mesh as well as the spectral discretization of SWAN.
467 Boundary conditions and directional spreading of the incident waves also
468 play a significant role when modeling wave-current interactions at meso-
469 and submesoscales (Villas Bôas et al., 2020), which motivated our choice
470 of imposing full spectra on the boundary of the wave model instead of
471 bulk parameters. Finally, SWAN default parameterizations for wind energy
472 input and whitecapping caused numerical instabilities by overestimating wave
473 growth and steepness on the boundary of the Gulf Stream on the passage
474 of Irma. This overestimation was solved by using the parameterization of
475 Siadatmousavi et al. (2011). The parameters used in this study were calibrated
476 on the Northern Gulf of Mexico conditions, which might explain that our
477 model better reproduces wave parameters at buoys located on the WFS.
478 However, these calibrated parameters might underestimate wind-induced
479 wave growth on Florida's eastern shelf. Consequently, incident wave do not
480 receive enough energy to grow after breaking on the bank boundary, leading to
481 an underestimation of the significant wave height at buoys located on Florida's
482 eastern shelf. A more extensive calibration study might therefore be necessary
483 to further improve the agreement with field measurements on both sides of
484 Florida. Nonetheless, as this study focuses on the wave produced by Irma,
485 which made landfall on the West coast of Florida, the use of parameterizations
486 calibrated for the Gulf of Mexico seems reasonable.

487 [add some words on limitations of model due to lack of 3D physics + heat

488 **flux to atmosphere]**

489 The radiation stress gradient significantly impacts currents during the
490 passage of the hurricane. It can induce differences of up to 1 m/s in the
491 current speed on the shelf break. In this region waves are strongly dissipated
492 due to action of depth-induced breaking and bottom dissipation on coral reefs.
493 This highlights the protective role of coral reefs against strong incoming waves
494 (Lowe et al., 2005), which requires a sufficiently fine spatial resolution to be
495 explicitly represented in the model. Due to the dissipation of incoming waves
496 on the reefs, wave impact during Irma is different on the inner and outer
497 shelves. It is less important on the inner shelf because of the sheltering of the
498 inner shelf due to reefs and islands as well as wave breaking on the shelf break.
499 The inner shelf hence experiences weaker waves and currents, inducing weaker
500 and more localized transport. Furthermore, the impact of winds on waves
501 is reduced in shallower areas under the action of depth-induced breaking.
502 This might explain why differences between particle trajectories stabilize
503 on the inner shelf just after the passage of Hurricane Irma. However, the
504 Florida Keys still experienced strong winds after the passage of the core of
505 the hurricane, which generated high waves in the deeper areas. This might
506 explain why the differences between the modeled trajectories kept increasing
507 on the outer shelf under the action of strong Stokes drift up to two days after
508 the passage of the hurricane.

509 The distance between the centers of mass of the particle clouds advected
510 by coupled and uncoupled Stokes drift remains rather limited (< 2 km). This
511 suggests that taking wave-current interactions into account when computing
512 Stokes drift, even in heavy wind conditions has a limited impact. Furthermore,
513 combining the coupled Stokes drift with the coupled and uncoupled SLIM
514 currents produced similar trajectories on the inner shelf, which seems to
515 indicate that wave impact on currents is limited in this region. This would
516 suggest that it is not necessary to take wave-current interactions into account
517 when modeling the trajectories of tracers in shallow, sheltered areas such

518 as the inner WFS during a hurricane. Uncoupled currents with uncoupled
519 Stokes drift should give a reasonably accurate approximation of the transport
520 processes. However, this does not hold for deeper and unsheltered regions,
521 as highlighted by the comparison of trajectories obtained with coupled and
522 uncoupled SLIM currents combined with coupled Stokes drift on the outer
523 shelf.

524 **5. Conclusion**

525 We developed a coupled wave-current model to study the impact of waves
526 on transport processes during Hurricane Irma. In order to accurately represent
527 the wind and pressure profiles of the hurricane, we built hybrid fields by
528 combining coarser ERA-5 data with high-resolution H*Wind data for the wind
529 speed and idealized Holland profiles for the pressure. Comparing these hybrid
530 profiles with field observations showed that they were better at reproducing the
531 observed central depression of the hurricane as well as the peak in wind speed
532 than ERA-5 data. Using these hybrid fields as forcings, our coupled model
533 accurately reproduced the storm surge at tide gauge locations and produced
534 currents and wave parameters in good agreement with field observations,
535 especially on the West Florida Shelf. The modeled currents and Stokes drift
536 were then used to evaluate the impact of waves on the trajectory of passive
537 drifters on the passage of the hurricane through the Florida Keys. Our results
538 show that waves had a significant impact on heavy-wind transport processes
539 and caused deflections of the drifters trajectories by more than 20 km on the
540 outer shelf.

541 Despite its good agreement with observations, our model could be fur-
542 ther refined by improving the representation of wind-wave interactions. In
543 particular, it does not consider the momentum loss due to the action of
544 surface waves when representing momentum flux from the atmosphere to the
545 ocean, leading to overestimations under hurricane conditions. Our model
546 could therefore be further improved by using wave-dissipative stress instead

547 of the full wind stress as the momentum flux from the atmosphere to the
548 ocean. Moreover, a more thorough calibration of the wave model parameters
549 should improve our model results on Florida's eastern shelf. Finally, as a 2D
550 barotropic model, SLIM does not explicitly represent baroclinic phenomena
551 as well as the vertical profile of the Stokes drift and radiation stress gradient
552 along the wave boundary layer. However, our study focused on relatively
553 shallow and vertically homogeneous coastal waters using a reef-scale resolution
554 throughout the whole FRT. Such fine resolution allows to explicitly represent
555 wave dissipation over coral reefs and is only achievable using a 2D model due
556 to computational resource limitations.

557 Wave coupling needs to be taken into account during heavy-wind events
558 but not necessarily in milder conditions. While the radiation stress gradient
559 plays an important role and can lead to differences of up to 5 km, the
560 Stokes drift is about 4 times more intense and should thus be considered
561 in priority. This study brings new insight on the impact of waves on the
562 transport processes nearshore during a tropical cyclone. Due to its high
563 spatial resolution, the developed coupled wave-current model can be used
564 to accurately represent the dispersal of pollutants, sediments or larvae in
565 topologically complex coastal areas in heavy-wind conditions.

566 Acknowledgments

567 Computational resources were provided by the Consortium des Équipements
568 de Calcul Intensif (CÉCI), funded by the F.R.S.-FNRS under Grant No.
569 2.5020.11. Thomas Dobbelaere is a PhD student supported by the Fund for
570 Research training in Industry and Agriculture (FRIA/FNRS).

571 This work was also supported by the Disaster Related Appropriation
572 Supplemental: Improving Forecasting and Assimilation (DRAS 19 IFAA),
573 awarded to the University of Miami under award NA19OAR0220184. It was
574 also supported by the FY19 Disaster Supplemental: Improving Forecasting of
575 Hurricanes, Floods, and Wildfires (FY19 IFHFW) awarded to the University

576 of Miami under award NA20OAR4600263. M. Le Hénaff received partial
577 support for work on this publication by NOAA/AOML, and was partly
578 supported under the auspices of the Cooperative Institute for Marine and
579 Atmospheric Studies (CIMAS), a cooperative institute of the University of
580 Miami and NOAA, cooperative agreement NA20OAR4320472.

581 **References**

- 582 Abdolali, A., Roland, A., Van Der Westhuysen, A., Meixner, J., Chawla,
583 A., Hesser, T.J., Smith, J.M., Sikiric, M.D., 2020. Large-scale hurricane
584 modeling using domain decomposition parallelization and implicit scheme
585 implemented in WAVEWATCH III wave model. Coastal Engineering 157,
586 103656.
- 587 Aijaz, S., Ghantous, M., Babanin, A., Ginis, I., Thomas, B., Wake, G., 2017.
588 Nonbreaking wave-induced mixing in upper ocean during tropical cyclones
589 using coupled hurricane-ocean-wave modeling. Journal of Geophysical
590 Research: Oceans 122, 3939–3963.
- 591 Bever, A.J., MacWilliams, M.L., 2013. Simulating sediment transport pro-
592 cesses in San Pablo Bay using coupled hydrodynamic, wave, and sediment
593 transport models. Marine Geology 345, 235–253.
- 594 Bhatia, K.T., Vecchi, G.A., Knutson, T.R., Murakami, H., Kossin, J., Dixon,
595 K.W., Whitlock, C.E., 2019. Recent increases in tropical cyclone intensifi-
596 cation rates. Nature Communications 10, 1–9.
- 597 Booij, N., Ris, R.C., Holthuijsen, L.H., 1999. A third-generation wave
598 model for coastal regions: 1. Model description and validation. Journal of
599 Geophysical Research: Oceans 104, 7649–7666.
- 600 Breivik, Ø., Allen, A.A., Maisondieu, C., Olagnon, M., 2013. Advances in
601 search and rescue at sea. Ocean Dynamics 63, 83–88.

- 602 Cangialosi, J.P., Latto, A.S., Berg, R., 2018. National Hurricane Center
603 Tropical Cyclone Report: Hurricane Irma (30 August12 September 2017).
604 https://www.nhc.noaa.gov/data/tcr/AL112017_Irma.pdf.
- 605 Chassignet, E.P., Hurlburt, H.E., Smedstad, O.M., Halliwell, G.R., Hogan,
606 P.J., Wallcraft, A.J., Baraille, R., Bleck, R., 2007. The HYCOM (hybrid
607 coordinate ocean model) data assimilative system. *Journal of Marine
608 Systems* 65, 60–83.
- 609 Craik, A.D., Leibovich, S., 1976. A rational model for Langmuir circulations.
610 *Journal of Fluid Mechanics* 73, 401–426.
- 611 Curcic, M., 2015. Explicit air-sea momentum exchange in coupled atmosphere-
612 wave-ocean modeling of tropical cyclones. Ph.D. thesis. University of Miami.
- 613 Curcic, M., Chen, S.S., Özgökmen, T.M., 2016. Hurricane-induced ocean
614 waves and stokes drift and their impacts on surface transport and dispersion
615 in the Gulf of Mexico. *Geophysical Research Letters* 43, 2773–2781.
- 616 Curcic, M., Haus, B.K., 2020. Revised estimates of ocean surface drag in
617 strong winds. *Geophysical Research Letters* 47, e2020GL087647.
- 618 Dietrich, J., Bunya, S., Westerink, J., Ebersole, B., Smith, J., Atkinson,
619 J., Jensen, R., Resio, D., Luettich, R., Dawson, C., et al., 2010. A high-
620 resolution coupled riverine flow, tide, wind, wind wave, and storm surge
621 model for southern Louisiana and Mississippi. Part II: Synoptic description
622 and analysis of Hurricanes Katrina and Rita. *Monthly Weather Review*
623 138, 378–404.
- 624 Dietrich, J., Westerink, J., Kennedy, A., Smith, J., Jensen, R., Zijlema, M.,
625 Holthuijsen, L., Dawson, C., Luettich, R., Powell, M., et al., 2011. Hurricane
626 Gustav (2008) waves and storm surge: Hindcast, synoptic analysis, and
627 validation in southern Louisiana. *Monthly Weather Review* 139, 2488–2522.

- 628 Dietrich, J.C., Tanaka, S., Westerink, J.J., Dawson, C., Luettich, R., Zijlema,
629 M., Holthuijsen, L.H., Smith, J., Westerink, L., Westerink, H., 2012. Performance of the unstructured-mesh, SWAN+ ADCIRC model in computing
630 hurricane waves and surge. *Journal of Scientific Computing* 52, 468–497.
- 632 Dobbelaere, T., Muller, E.M., Gramer, L.J., Holstein, D.M., Hanert, E., 2020.
633 Coupled epidemic-hydrodynamic modeling to understand the spread of a
634 deadly coral disease in Florida. *Frontiers in Marine Science* 7, 1016.
- 635 Donelan, M., Haus, B., Reul, N., Plant, W., Stiassnie, M., Graber, H., Brown,
636 O., Saltzman, E., 2004. On the limiting aerodynamic roughness of the
637 ocean in very strong winds. *Geophysical Research Letters* 31.
- 638 Drivdal, M., Broström, G., Christensen, K., 2014. Wave-induced mixing and
639 transport of buoyant particles: Application to the Statfjord A oil spill.
640 *Ocean Science* 10, 977–991.
- 641 Ezer, T., 2018. On the interaction between a hurricane, the Gulf Stream and
642 coastal sea level. *Ocean Dynamics* 68, 1259–1272.
- 643 Ezer, T., Atkinson, L.P., Tuleya, R., 2017. Observations and operational
644 model simulations reveal the impact of Hurricane Matthew (2016) on the
645 Gulf Stream and coastal sea level. *Dynamics of Atmospheres and Oceans*
646 80, 124–138.
- 647 Figueiredo, J., Baird, A.H., Connolly, S.R., 2013. Synthesizing larval com-
648 petence dynamics and reef-scale retention reveals a high potential for
649 self-recruitment in corals. *Ecology* 94, 650–659.
- 650 Fringer, O.B., Dawson, C.N., He, R., Ralston, D.K., Zhang, Y.J., 2019. The
651 future of coastal and estuarine modeling: Findings from a workshop. *Ocean
652 Modelling* 143, 101458.
- 653 Frys, C., Saint-Amand, A., Le Hénaff, M., Figueiredo, J., Kuba, A., Walker,
654 B., Lambrechts, J., Vallaeys, V., Vincent, D., Hanert, E., 2020. Fine-scale

- 655 coral connectivity pathways in the Florida Reef Tract: Implications for
656 conservation and restoration. *Frontiers in Marine Science* 7, 312.
- 657 Geuzaine, C., Remacle, J.F., 2009. Gmsh: A 3-d finite element mesh generator
658 with built-in pre-and post-processing facilities. *International journal for
659 numerical methods in engineering* 79, 1309–1331.
- 660 Harper, B., Kepert, J., Ginger, J., 2010. Guidelines for converting between
661 various wind averaging periods in tropical cyclone conditions.
- 662 Hegermiller, C.A., Warner, J.C., Olabarrieta, M., Sherwood, C.R., 2019.
663 Wave-current interaction between Hurricane Matthew wave fields and the
664 Gulf Stream. *Journal of Physical Oceanography* 49, 2883–2900.
- 665 Hoefel, F., Elgar, S., 2003. Wave-induced sediment transport and sandbar
666 migration. *Science* 299, 1885–1887.
- 667 Holthuijsen, L.H., Powell, M.D., Pietrzak, J.D., 2012. Wind and waves in
668 extreme hurricanes. *Journal of Geophysical Research: Oceans* 117.
- 669 Janssen, P.A., 1991. Quasi-linear theory of wind-wave generation applied to
670 wave forecasting. *Journal of Physical Oceanography* 21, 1631–1642.
- 671 Johns, W.E., Schott, F., 1987. Meandering and transport variations of the
672 Florida Current. *Journal of Physical Oceanography* 17, 1128–1147.
- 673 Knaff, J.A., Sampson, C.R., Musgrave, K.D., 2018. Statistical tropical cyclone
674 wind radii prediction using climatology and persistence: Updates for the
675 western North Pacific. *Weather and Forecasting* 33, 1093–1098.
- 676 Komen, G., Hasselmann, S., Hasselmann, K., 1984. On the existence of a
677 fully developed wind-sea spectrum. *Journal of Physical Oceanography* 14,
678 1271–1285.

- 679 Kossin, J.P., Knapp, K.R., Olander, T.L., Velden, C.S., 2020. Global increase
680 in major tropical cyclone exceedance probability over the past four decades.
681 Proceedings of the National Academy of Sciences 117, 11975–11980.
- 682 Kourafalou, V.H., Kang, H., 2012. Florida Current meandering and evo-
683 lution of cyclonic eddies along the Florida Keys Reef Tract: Are they
684 interconnected? Journal of Geophysical Research: Oceans 117.
- 685 Kundu, P.K., 1976. Ekman veering observed near the ocean bottom. Journal
686 of Physical Oceanography 6, 238–242.
- 687 Lambrechts, J., Hanert, E., Deleersnijder, E., Bernard, P.E., Legat, V.,
688 Remacle, J.F., Wolanski, E., 2008. A multi-scale model of the hydrodynam-
689 ics of the whole Great Barrier Reef. Estuarine, Coastal and Shelf Science
690 79, 143–151.
- 691 Landsea, C.W., Franklin, J.L., 2013. Atlantic hurricane database uncertainty
692 and presentation of a new database format. Monthly Weather Review 141,
693 3576–3592.
- 694 Lane, E.M., Restrepo, J., McWilliams, J.C., 2007. Wave–current interaction:
695 A comparison of radiation-stress and vortex-force representations. Journal
696 of Physical Oceanography 37, 1122–1141.
- 697 Langmuir, I., 1938. Surface motion of water induced by wind. Science 87,
698 119–123.
- 699 Le, H.A., Lambrechts, J., Ortaleb, S., Gratiot, N., Deleersnijder, E., Soares-
700 Frazão, S., 2020. An implicit wetting–drying algorithm for the discontinuous
701 galerkin method: application to the tonle sap, mekong river basin. Envi-
702 ronmental Fluid Mechanics , 1–29.
- 703 Le Hénaff, M., Kourafalou, V.H., Paris, C.B., Helgers, J., Aman, Z.M., Hogan,
704 P.J., Srinivasan, A., 2012. Surface evolution of the Deepwater Horizon

- 705 oil spill patch: Combined effects of circulation and wind-induced drift.
706 Environmental Science & Technology 46, 7267–7273.
- 707 Lee, T.N., Leaman, K., Williams, E., Berger, T., Atkinson, L., 1995. Florida
708 Current meanders and gyre formation in the southern Straits of Florida.
709 Journal of Geophysical Research: Oceans 100, 8607–8620.
- 710 Lee, T.N., Mayer, D.A., 1977. Low-frequency current variability and spin-off
711 eddies along the shelf off southeast Florida. Collected Reprints 1, 344.
- 712 Lee, T.N., Smith, N., 2002. Volume transport variability through the Florida
713 Keys tidal channels. Continental Shelf Research 22, 1361–1377.
- 714 Lee, T.N., Williams, E., 1988. Wind-forced transport fluctuations of the
715 Florida Current. Journal of Physical Oceanography 18, 937–946.
- 716 Li, Z., Johns, B., 1998. A three-dimensional numerical model of surface
717 waves in the surf zone and longshore current generation over a plane beach.
718 Estuarine, Coastal and Shelf Science 47, 395–413.
- 719 Lin, N., Chavas, D., 2012. On hurricane parametric wind and applications in
720 storm surge modeling. Journal of Geophysical Research: Atmospheres 117.
- 721 Liu, Y., Weisberg, R.H., 2012. Seasonal variability on the West Florida shelf.
722 Progress in Oceanography 104, 80–98.
- 723 Liu, Y., Weisberg, R.H., Zheng, L., 2020. Impacts of hurricane Irma on the
724 circulation and transport in Florida Bay and the Charlotte Harbor estuary.
725 Estuaries and Coasts 43, 1194–1216.
- 726 Liubartseva, S., Coppini, G., Lecci, R., Clementi, E., 2018. Tracking plastics
727 in the Mediterranean: 2D Lagrangian model. Marine Pollution Bulletin
728 129, 151–162.
- 729 Longuet-Higgins, M.S., 1970. Longshore currents generated by obliquely
730 incident sea waves. Journal of Geophysical Research 75, 6778–6789.

- 731 Longuet-Higgins, M.S., Stewart, R., 1964. Radiation stresses in water waves;
732 a physical discussion, with applications, in: Deep Sea Research and Oceano-
733 graphic Abstracts, Elsevier. pp. 529–562.
- 734 Lowe, R.J., Falter, J.L., Bandet, M.D., Pawlak, G., Atkinson, M.J., Moni-
735 smith, S.G., Koseff, J.R., 2005. Spectral wave dissipation over a barrier
736 reef. Journal of Geophysical Research: Oceans 110.
- 737 Madsen, O.S., Poon, Y.K., Gruber, H.C., 1989. Spectral wave attenuation by
738 bottom friction: Theory, in: Coastal Engineering 1988, pp. 492–504.
- 739 Malmstadt, J., Scheitlin, K., Elsner, J., 2009. Florida hurricanes and damage
740 costs. Southeastern Geographer 49, 108–131.
- 741 Mao, M., Xia, M., 2018. Wave-current dynamics and interactions near the
742 two inlets of a shallow lagoon-inlet-coastal ocean system under hurricane
743 conditions. Ocean Modelling 129, 124–144.
- 744 Mao, M., Xia, M., 2020. Particle dynamics in the nearshore of Lake Michi-
745 gan revealed by an observation-modeling system. Journal of Geophysical
746 Research: Oceans 125, e2019JC015765.
- 747 McWilliams, J.C., Restrepo, J.M., Lane, E.M., 2004. An asymptotic theory
748 for the interaction of waves and currents in coastal waters. Journal of Fluid
749 Mechanics 511, 135.
- 750 McWilliams, J.C., Sullivan, P.P., 2000. Vertical mixing by Langmuir circula-
751 tions. Spill Science & Technology Bulletin 6, 225–237.
- 752 Mei, C.C., 1989. The applied dynamics of ocean surface waves. volume 1.
753 World scientific.
- 754 Moon, I.J., Ginis, I., Hara, T., Thomas, B., 2007. A physics-based parame-
755 terization of air-sea momentum flux at high wind speeds and its impact on
756 hurricane intensity predictions. Monthly Weather Review 135, 2869–2878.

- 757 Niu, Q., Xia, M., 2017. The role of wave-current interaction in Lake Erie's
758 seasonal and episodic dynamics. *Journal of Geophysical Research: Oceans*
759 122, 7291–7311.
- 760 Oey, L.Y., Ezer, T., Wang, D.P., Yin, X.Q., Fan, S.J., 2007. Hurricane-
761 induced motions and interaction with ocean currents. *Continental Shelf*
762 *Research* 27, 1249–1263.
- 763 Pinelli, J.P., Roueche, D., Kijewski-Correa, T., Plaz, F., Prevatt, D., Zisis,
764 I., Elawady, A., Haan, F., Pei, S., Gurley, K., et al., 2018. Overview of
765 damage observed in regional construction during the passage of Hurricane
766 Irma over the State of Florida, in: *Forensic Engineering 2018: Forging*
767 *Forensic Frontiers*. American Society of Civil Engineers Reston, VA, pp.
768 1028–1038.
- 769 Powell, M.D., Houston, S.H., Amat, L.R., Morisseau-Leroy, N., 1998. The
770 HRD real-time hurricane wind analysis system. *Journal of Wind Engineering*
771 and Industrial Aerodynamics 77, 53–64.
- 772 Powell, M.D., Vickery, P.J., Reinhold, T.A., 2003. Reduced drag coefficient
773 for high wind speeds in tropical cyclones. *Nature* 422, 279–283.
- 774 Röhrs, J., Christensen, K.H., Hole, L.R., Broström, G., Drivdal, M., Sundby,
775 S., 2012. Observation-based evaluation of surface wave effects on currents
776 and trajectory forecasts. *Ocean Dynamics* 62, 1519–1533.
- 777 Schott, F.A., Lee, T.N., Zantopp, R., 1988. Variability of structure and
778 transport of the Florida Current in the period range of days to seasonal.
779 *Journal of Physical Oceanography* 18, 1209–1230.
- 780 Siadatmousavi, S.M., Jose, F., Stone, G., 2011. Evaluation of two WAM
781 white capping parameterizations using parallel unstructured SWAN with
782 application to the Northern Gulf of Mexico, USA. *Applied Ocean Research*
783 33, 23–30.

- 784 Sikirić, M.D., Roland, A., Janeković, I., Tomazić, I., Kuzmić, M., 2013.
785 Coupling of the Regional Ocean Modeling System (ROMS) and Wind
786 Wave Model. *Ocean Modelling* 72, 59–73.
- 787 Smith, N.P., 1982. Response of Florida Atlantic shelf waters to hurricane
788 David. *Journal of Geophysical Research: Oceans* 87, 2007–2016.
- 789 Spivakovskaya, D., Heemink, A., Milstein, G., Schoenmakers, J., 2005. Sim-
790 ulation of the transport of particles in coastal waters using forward and
791 reverse time diffusion. *Advances in water resources* 28, 927–938.
- 792 Stokes, G.G., 1880. On the theory of oscillatory waves. *Transactions of the*
793 *Cambridge Philosophical Society* .
- 794 Tolman, H.L., et al., 2009. User manual and system documentation of
795 WAVEWATCH III TM version 3.14. Technical note, MMAB Contribution
796 276, 220.
- 797 Van Den Bremer, T., Breivik, Ø., 2018. Stokes drift. *Philosophical Trans-*
798 *actions of the Royal Society A: Mathematical, Physical and Engineering*
799 *Sciences* 376, 20170104.
- 800 Varlas, G., Vervatis, V., Spyrou, C., Papadopoulou, E., Papadopoulos, A.,
801 Katsafados, P., 2020. Investigating the impact of atmosphere–wave–ocean
802 interactions on a Mediterranean tropical-like cyclone. *Ocean Modelling* 153,
803 101675.
- 804 Villas Bôas, A.B., Cornuelle, B.D., Mazloff, M.R., Gille, S.T., Arduin, F.,
805 2020. Wave–current interactions at meso-and submesoscales: Insights from
806 idealized numerical simulations. *Journal of Physical Oceanography* 50,
807 3483–3500.
- 808 Wachnicka, A., Browder, J., Jackson, T., Louda, W., Kelble, C., Abdelrahman,
809 O., Stabenau, E., Avila, C., 2019. Hurricane Irmas impact on water quality

- 810 and phytoplankton communities in Biscayne Bay (Florida, USA). *Estuaries*
811 and Coasts , 1–18.
- 812 WAMDI Group, 1988. The WAM model – A third generation ocean wave
813 prediction model. *Journal of Physical Oceanography* 18, 1775–1810.
- 814 Warner, J.C., Armstrong, B., He, R., Zambon, J.B., 2010. Development of a
815 coupled ocean–atmosphere–wave–sediment transport (COAWST) modeling
816 system. *Ocean modelling* 35, 230–244.
- 817 Weisberg, R., Liu, Y., Mayer, D., 2009. Mean circulation on the west Florida
818 continental shelf observed with long-term moorings. *Geophys. Res. Lett*
819 36, L19610.
- 820 Weisberg, R.H., Zheng, L., 2006. Hurricane storm surge simulations for
821 Tampa Bay. *Estuaries and Coasts* 29, 899–913.
- 822 Wu, L., Chen, C., Guo, P., Shi, M., Qi, J., Ge, J., 2011. A FVCOM-
823 based unstructured grid wave, current, sediment transport model, I. Model
824 description and validation. *Journal of Ocean University of China* 10, 1–8.
- 825 WW3DG, 2019. User Manual and System Documentation of WAVEWATCH
826 III Version 6.07, the WAVEWATCH III Development Group. Technical Note
827 316. NOAA/NWS/ NCEP/MMAB url: <https://github.com/NOAA-EMC/WW3/wiki/files/manual.pdf>.
- 828 Xian, S., Feng, K., Lin, N., Marsooli, R., Chavas, D., Chen, J., Hatzikyriakou,
829 A., 2018. Brief communication: Rapid assessment of damaged residential
830 buildings in the Florida Keys after Hurricane Irma. *Natural Hazards and*
831 *Earth System Sciences* 18, 2041–2045.
- 832 Zedler, S., Niiler, P., Stammer, D., Terrill, E., Morzel, J., 2009. Ocean's
833 response to Hurricane Frances and its implications for drag coefficient
834 parameterization at high wind speeds. *Journal of Geophysical Research:*
835 *Oceans* 114.

837 Zhang, C., Durgan, S.D., Lagomasino, D., 2019. Modeling risk of mangroves
838 to tropical cyclones: A case study of Hurricane Irma. *Estuarine, Coastal*
839 and Shelf Science 224, 108–116.